Effect of 1 wt% LiF additive on the densification of nanocrystalline Y_2O_3 ceramics by spark plasma sintering

Rachel Marder [a], Rachman Chaim [a,*], Geoffroy Chevallier [b], Claude Estournès [b]

[a] *Department of Materials Engineering, Technion – Israel Institute of Technology, Haifa 32000, Israel*
[b] *CNRS, Institut Carnot Cirimat, F-31602 Toulouse Cedex 9, France*

Abstract

Densification of nanocrystalline cubic yttria (nc-Y_2O_3) powder, with 18 nm crystal size and 1 wt% LiF as a sintering additive was investigated. Specimens were fabricated by spark plasma sintering at 100 MPa, within the temperature range of 700–1500 °C. Sintering at 700 °C for 5 and 20 min resulted in 95% and 99.7% dense specimens, with an average grain size of 84 and 130 nm, respectively. nc-Y_2O_3 without additive was only 65% dense at 700 °C for 5 min. The presence of LiF at low sintering temperatures facilitated rapid densification by particle sliding and jamming release. Sintering at high temperatures resulted in segregation of LiF to the grain boundaries and its entrapment as globular phase within the fast growing Y_2O_3 grains. The sintering enhancement advantage of LiF was lost at high SPS temperatures.

1. Introduction

Spark plasma sintering (SPS) has been used for rapid densification of different ceramic compositions to full density at moderate temperatures.[1–5] The rapid densification has been mainly related either to plastic deformation or particle sliding at the first and the second stages of sintering, hence significant effect is attributed to the interfacial processes. Therefore, ceramic nano-powders are excellent candidates for densification by SPS due to their large specific surface area. SPS was successfully used for the fabrication of both nanocrystalline and optically transparent ceramics.[6–11] The main drawback of the SPS technique lies in the application of graphite as the conducting dies and plungers which form a carbonic atmosphere during densification of the powder compact. The dissolved or entrapped gas may introduce physical defects as well as chemical composition changes in the compact, hence affect its densification behavior[12] and especially degrade its optical properties.[13]

Alkali halides have long been recognized as effective sintering aids towards optically transparent polycrystalline ceramics. LiF was used as a sintering aid for fabrication of transparent oxides.[14–17] Different functionalities were tailored to LiF additives such as grain boundary liquid phase formation for diffusion enhancement, increasing the oxygen vacancies and thus the volume diffusion, low-solubility such that it segregates into isolated pockets during the cooling, and finally reaction with the impurities.[18] These functionalities were also used for rapid densification of transparent spinel[19] and YAG[20] by the SPS process. Nevertheless, excess LiF additive was found to degrade the chemical stability of the spinel.[21] LiF vapor was suggested to eliminate the carbon by forming a volatile carbon–fluoride gas during the SPS processing of the spinel.[19] LiF additives were effective during vacuum hot-pressing of conventional size Y_2O_3 powders towards transparent ceramics.[21–23] The yield stress for plastic deformation in LiF polycrystal is 14 MPa at 350 °C and less than 3.5 MPa at 600 °C,[24] which assures easy flow of this additive under the relatively high pressures applied during the SPS.

Recently, densification of pure nc-Y_2O_3 powders by SPS at different temperatures was investigated.[25–28] SPS of 18 nm Y_2O_3 particles for 10 min at 1100 °C resulted in 95% dense nanocrystalline ceramics with ∼100 nm grains.[25,26] Different

* Corresponding author. Tel.: +972 4 8294589; fax: +972 4 8295677.
 E-mail addresses: rchaim@technion.ac.il, rchaim@tx.technion.ac.il
(R. Chaim).

nanocrystalline yttria but with similar particle size was sintered for 1 h at the lower temperature of 850 °C to 97% density and 500 nm grain size.[27] However, at lower sintering temperature of 700 °C, the corresponding densities were below 70%. In the present work, the effect of 1 wt% LiF additive on densification behavior and microstructure evolution of nanocrystalline yttrium oxide (nc-Y_2O_3) was investigated.

2. Experimental procedure

Pure nanocrystalline Y_2O_3 (nc-Y_2O_3, 99.99%, Cathay Advanced Materials, China) with 18 nm mean crystallite size (diameter) and micrometer size cubic LiF crystals (99.995%, Sigma–Aldrich) as a sintering additive were used. The as-received nc-Y_2O_3 powder was dry mixed with 1 wt% LiF powder using zirconia ball mills for 15 min. Discs of 8 mm in diameter and 1.6–2.6 in thickness were fabricated using the SPS unit (Dr. Sinter, SPS 2080) of the Plateforme Nationale de Frittage Flash (PNF2) du CNRS located at Toulouse. The powders were poured and pressed in a graphite die; the powder was isolated by graphite foils from the die wall and plunger surfaces. Different SPS modes were used to reveal the various effects of the LiF additive on the densification behavior. The starting temperature was either room temperature (mode 1) or 600 °C (mode 2), using a heating rate of 100 °C/min. Specimens were sintered at four different temperatures; 700 °C and 1000 °C using mode 1, and 1200 °C and 1500 °C using mode 2. In mode 1, the temperature was raised 2 and 6 min after the process began, for the LiF-added and the pure nc-Y_2O_3 powder, respectively. A thermocouple was used to control the temperature increase to 600 °C (mode 1), and further temperature increase (mode 2) was monitored by an optical pyrometer focused on a small hole located at the surface of the die. A pulsed DC current density (up to 200 A cm^{-2}) of 3.3 ms pulse duration was used. A vacuum level of 2–3 Pa was maintained during the SPS process. The pressure in the LiF-added powders sintered at 1500 °C was applied either at 600 °C or at 1500 °C, for comparison. The process duration was 5 min from the time the SPS temperature was reached. The applied uniaxial pressure was increased linearly to reach 100 MPa within 100–150 s from the process start, and held until the end of the heating. In addition, LiF-added nc-Y_2O_3 powders were sintered at 700 °C for different durations (5, 10 and 20 min). The SPS parameters such as temperature, pressure, duration, ram displacement and its rate, and the vacuum level were recorded versus the process time. The following equations and data were used to determine the temporary relative density versus time. The temporary relative density ρ is expressed by:

$$\rho = \rho_0 \left(1 + \frac{\Delta V}{V}\right) \tag{1}$$

where ρ_0 is the green density, V is the temporary specimen volume and ΔV is the volume change. For uniaxial hot-pressing where the specimen diameter is assumed to be constant, and following engineering strains, Eq. (1) can be modified to:

$$\rho = \rho_0 \left(1 + \frac{\Delta h - \Delta h_{\text{therm}}}{h_0 - (\Delta h - \Delta h_{\text{therm}})}\right) \tag{2}$$

where h_0 is thickness of the green specimen, Δh is the recorded ram displacement, and Δh_{therm} is the ram displacement due to thermal expansions of the specimen and the graphite die (measured during the cooling).

The difference ($\Delta h - \Delta h_{\text{therm}}$) in Eq. (2) is the linear shrinkage in the specimen thickness due to the densification process. The relation between the two thicknesses and the two displacements is given by:

$$h_0 = h + \Delta h - \Delta h_{\text{therm}} \tag{3}$$

where h is the temporary specimen thickness.

The shrinkage rate was calculated using $\left[(\Delta h - \Delta h_{\text{therm}})/h\right](1/60\Delta t)$ where $(\Delta h - \Delta h_{\text{therm}})/\Delta t$ [mm/min] is the recorded ram displacement rate.

The density of the sintered specimens was measured by the Archimedes method (ASTM standard C 20-92) with an accuracy of ±0.5% using distilled water medium. X-ray diffraction (XRD, Philips PW 3710 diffractometer) was used for phase identification at two different scanning rates: 0.45°/min in the 2θ range (θ is the Bragg diffraction angle) between 15 and 70°, and 0.06°/min between 35 and 46°. The specimens for Scanning Electron Microscopy (FEI E-SEM Quanta 200, operated at 20 kV) observations were prepared by mechanical polishing with diamond pastes down to 0.5 μm and thermal etching for 20 min in air at temperatures lower by 100 °C than the corresponding SPS temperature. The specimens for Transmission Electron Microscopy (TEM, FEI Tecnai G^2 T20, operated at 200 kV) observations were prepared by conventional mechanical and ion milling to electron transparency. About 200 grains were counted in each specimen for grain size statistics, using the largest axis of the grain, using SEM and TEM images, for micrometer and sub-micrometer grain size analyses, respectively. The standard deviations in the particle size distributions were typically wide, 50% of the average grain size. Differential Scanning Calorimeter (Labsys 1600, Setaram) was used to characterize the thermal behavior of the pure and LiF-added powders, using a heating rate of 10 °C min^{-1}.

3. Results

The as-received nc-Y_2O_3 powder has been characterized in previous works, using XRD and TEM.[25,26] X-ray diffraction spectra from the pure nc-Y_2O_3, and 1 wt% LiF-added nc-Y_2O_3 powder showed the cubic crystal structure of Y_2O_3 and confirmed the presence of the LiF additive by two small but distinct peaks (indexed peaks in Fig. 1b); the latter were related to (1 1 1) and (2 0 0) reflections, the most intense peaks of cubic LiF. The resolved LiF diffraction peaks, albeit its low volume fraction (2%), can be related to the relatively large size of its crystals dispersed within the nanocrystalline Y_2O_3 powder. Clear broadening of the Y_2O_3 peaks from the as-received powder was visible, resulting from its nanocrystalline character (Fig. 1a and b). The LiF peak was still present after SPS at 700 °C (Fig. 1c). However, the Y_2O_3 peak widths become narrower after the 700 °C treatment, indicating the presence of some particle coarsening and grain growth during the densifica-
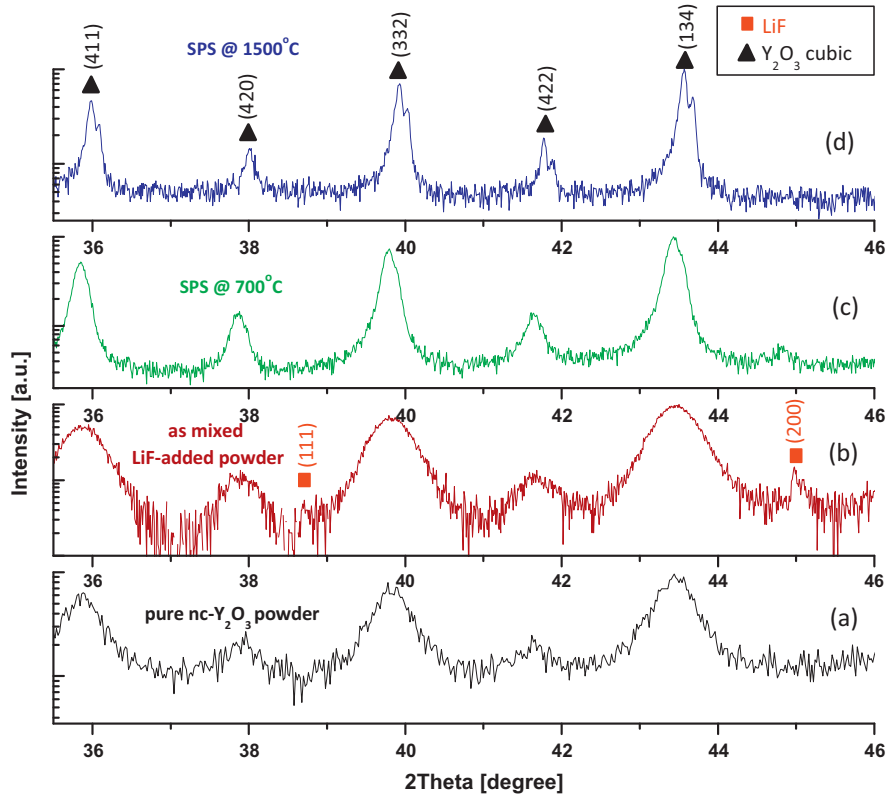
Fig. 1. X-ray diffraction spectra from (a) pure nc-Y_2O_3, (b) as mixed nc-Y_2O_3 + 1 wt% LiF powder, and after SPS for 5 min at (c) 700 °C and (d) 1500 °C. LiF peaks (red squares); cubic Y_2O_3 peaks (black triangles). The intensity was plotted on a logarithmic scale to highlight the faint LiF peaks. (For interpretation of the references to colour in this figure legend, the reader is referred to the web version of this article.)

tion. Yet, in the diffraction spectrum of the specimen after SPS at 1500 °C, no visible LiF peaks were detected. This particle coarsening at 700 °C can be related to the activated surfaces of the nano-particles due to the presence of LiF with carbonic gas, and is discussed below. The relatively narrow diffraction peaks observed from the specimen sintered at 1500 °C (Fig. 1d) were indicative of the significant grain growth which occurred during the SPS process, leading to loss of the nanocrystalline character. Narrowing of the peak width also resolved the diffraction peak originating from the Kα_2 radiation. SPS of similar pure nc-Y_2O_3 nanopowder at 1500 °C and 180 °C min^{-1} heating rate resulted in an average grain size of 5.5 ± 2.0 μm compared to 2.5 μm in the present experiments (heating rate of 100 °C min^{-1}).[26]

The changes in the relative density, temperature, and pressure versus the SPS duration for selected specimens were plotted in Figs. 2 and 3. The green density was around 30%. The relative density of pure nc-Y_2O_3 specimens sintered at 700 °C (Fig. 2a) and 1000 °C (Fig. 2b) increased with the pressure application and stabilized around 42–44% when the desired pressure of 100 MPa was reached after 2 min. It should be noted that no further densification was observed prior to the heating start. Therefore, the observed densification is related to rearrangement and sliding of the particles during the cold compaction. The temperature increase, which began about 6 min after the process start, led to further increase in the relative density up to 65% and 93.5% at 700 °C and 1000 °C, respectively. The corresponding shrinkage rate for the 700 °C treatment increased from

4×10^{-4} s^{-1} to 2.1×10^{-3} s^{-1} near 680 °C. However, the relative density seemed to stabilize at 700 °C, and an increase of only a few percents was recorded during this isotherm. In the case of pure nc-Y_2O_3 specimen sintered at 1000 °C (Fig. 2b), the highest shrinkage rate ($\sim2.1 \times 10^{-3}$ s^{-1}) was similarly reached at 680 °C and persisted up to 880 °C. The densification ceased above 880 °C, before reaching the final SPS temperature.

The corresponding relative density curves of the 1 wt% LiF-added nc-Y_2O_3 specimens sintered at 700 °C (Fig. 2c) and 1000 °C (Fig. 2d) exhibited similar trends (as mentioned above), albeit with two main differences. First, the temperature was increased immediately after the maximum pressure was reached. Still, the density increased negligibly during the heating (at the first 5 min) under constant pressure. Second, in both treatments, the temperature at which the maximum shrinkage rate started (~600 °C) was lower by 80 °C than that observed for the pure nc-Y_2O_3 specimens. The highest shrinkage rates for the LiF-added specimens sintered at 700 °C and 1000 °C were 4.1×10^{-3} s^{-1} and 4.5×10^{-3} s^{-1}, respectively, higher by more than two times than measured for the counterpart pure nc-Y_2O_3 compacts. It is of noteworthy that the relative densities in the pure nc-Y_2O_3 specimens at 700 °C and 1000 °C were 65% and 93.5%, respectively, compared to 95% and 95.3% in their LiF-added counterpart specimens. Again, no noticeable densification was observed at the isotherms.

The relative density curves of the LiF-added nc-Y_2O_3 specimen sintered by mode 2 at 1500 °C showed a high degree of
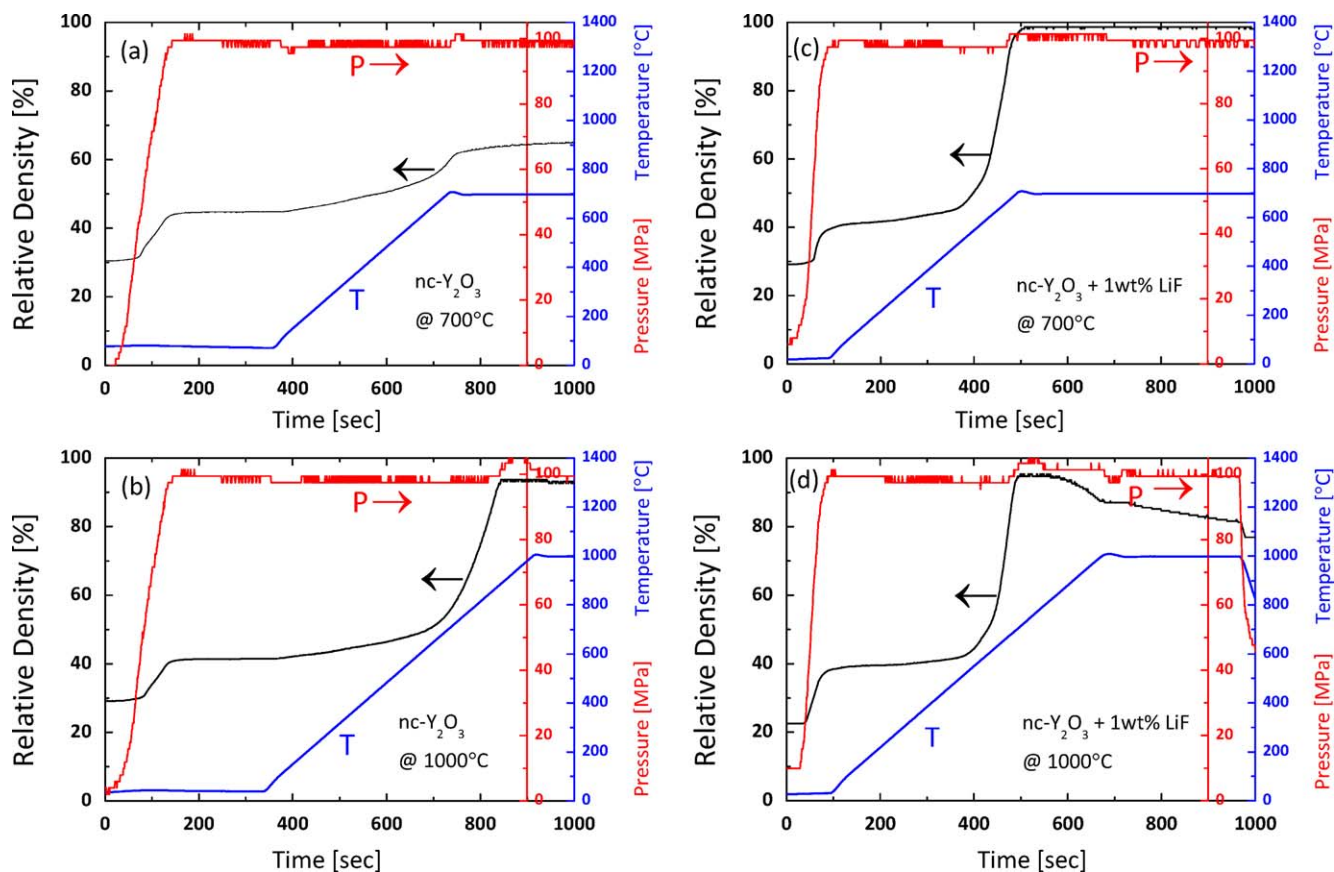
Fig. 2. Relative density versus process temperature, pressure and time. Pure nc-Y_2O_3 after SPS at (a) 700 °C and (b) 1000 °C. 1 wt% LiF-added nc-Y_2O_3 sintered at (c) 700 °C, and (d) 1000 °C.

densification at the heating pulse (∼100 s) while under 50 MPa pressure, before reaching the maximal pressure (Fig. 3a). Another run has been performed with a similar thermal cycle but with pressure only applied at the SPS isotherm (Fig. 3b). Even though the pressure was negligible (6–12 MPa) during the temperature increase, a significant densification started already at 700 °C and reached 77% at ∼1000 °C. These experiments revealed the strong effect of the capillary forces due to the high specific surface area of the nanocrystalline powder, aided by the presence of viscous LiF as discussed below. The maximum shrinkage rates determined around the inflection points of the density curves were $2.6 \times 10^{-2}\,s^{-1}$ and $5.4 \times 10^{-3}\,s^{-1}$, with and without pressure application, respectively.

It was found that ∼3 min after the SPS process had started, the LiF-added nc-Y_2O_3 specimen reached over 95% final density under 100 MPa with a heat pulse at 600 °C (Fig. 3a). The cause for the decrease in the relative density at longer durations may be associated with the thermal expansion mismatch between the dense specimen and the graphite plungers; it ceased at the end of the heating stage. Some chemical reaction of LiF with carbon and gas formation may also be present.[18]

Important densification behavior was noted in pure nc-Y_2O_3 heated to 1500 °C (Fig. 3c). Densification started with the pressure increase and continued with a heat pulse at 600 °C; it ceased at a relative density of 62% when the maximum applied pressure of 100 MPa was reached at 600 °C (200 s in Fig. 3c). Further

increase in temperature at constant pressure did not contribute to further densification. Nevertheless, occasional pressure release (at 400 and 580 s in Fig. 3c) and reload steps (at 450 and 610 s in Fig. 3c) led to further increase in the relative density to 77% and 98%, respectively. This effect revealed the jamming tendency of the pure nc-Y_2O_3 powder during the compaction, even at very high temperatures. Any change in the stress distribution in the jammed powder compact (i.e., pressure release and reload) is expected to release the jamming (until the buildup of the next jam).[29,30] Jam release initiated by decrease in the applied pressure is associated with negligible shrinkage, due to the elastic nature of the jamming. Only after reloading, the particle sliding can contribute to further shrinkage, hence further densification, as observed. This is in strong contrast to the easy compaction and high shrinkage rate of the LiF-added counterpart specimen (Fig. 3a), revealing the strong lubricating effect of LiF on the compact densification.

The relative densities of the different specimens versus the SPS temperature are shown in Fig. 4. Generally, all densities increased with the SPS temperature increase, in contrast to the density decrease observed above 1400 °C, when a heating rate of 180 °C min^{-1} was used.[25] However, the main point of this plot is the significant increase in the density of the LiF-added specimens already at 700 °C (95%), compared to pure nc-Y_2O_3 (65%). At higher SPS temperatures, the density of the LiF-added specimen is higher only by a few percents than that of pure nc-
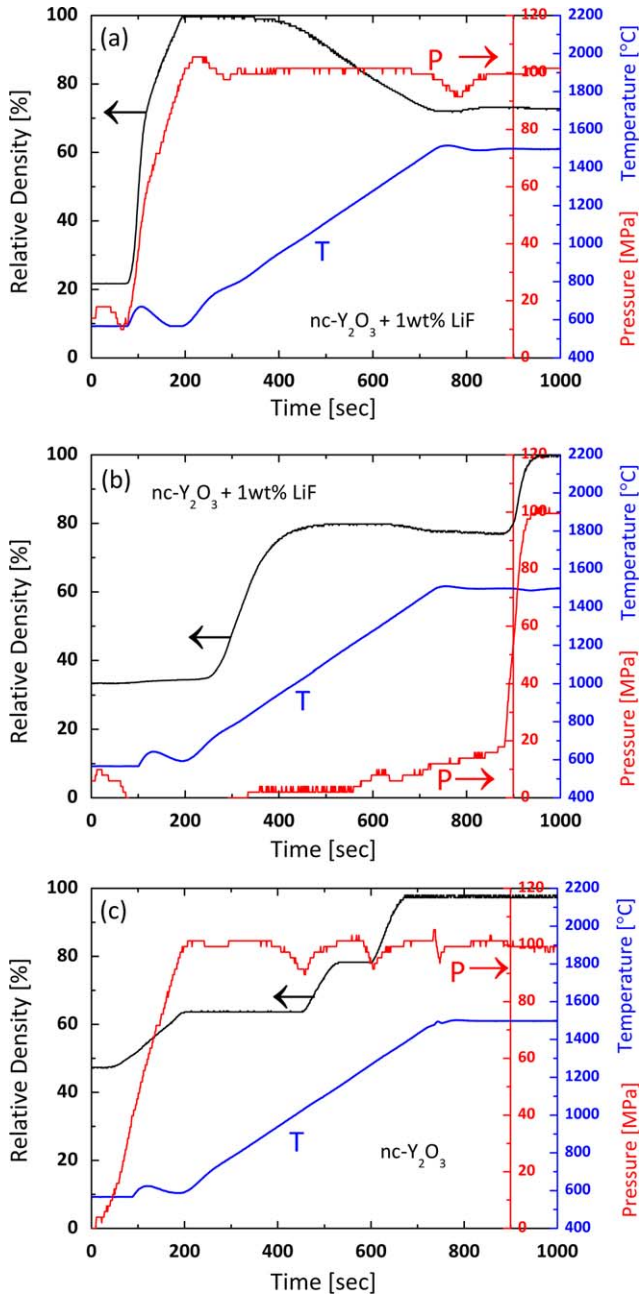
Fig. 3. Relative density versus process temperature, pressure and time for sintering at 1500 °C and different pressure application regimes. (a) and (b) 1 wt% LiF-added nc-Y_2O_3 and (c) pure nc-Y_2O_3.

Y_2O_3. Further increase in the SPS duration to 20 min at 700 °C resulted in a relative density of 99.7%, with an average grain size of 130 nm. On the other hand, the average grain size measured versus the SPS temperatures exhibited significant grain growth with the temperature increase in the LiF-added specimens (Fig. 5); the average grain size increased from 84 ± 30 nm at 700 °C to 17 ± 10 μm at 1500 °C.

TEM images of the LiF-added specimen sintered at 700 °C revealed some micrometer size elongated grains (Fig. 6a) in the otherwise relatively homogeneous nanostructure matrix with equiaxed grains, smaller than 200 nm in diameter (Fig. 6b). Microchemical composition analysis by EDS of the elongated
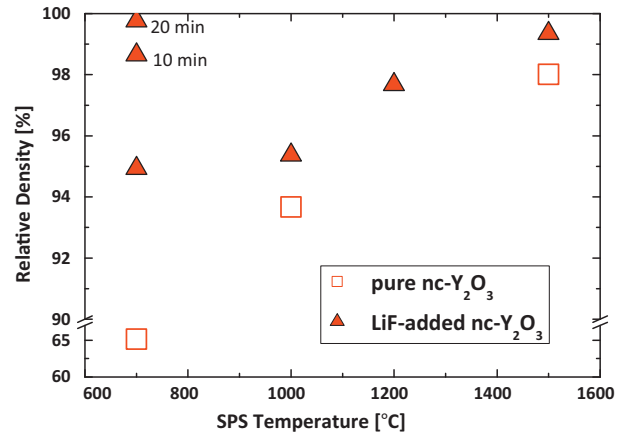

Fig. 4. Relative density after 5 min at the SPS temperature showing a significant increase in the density of 1 wt% LiF-added nc-Y_2O_3 at 700 °C. The accuracy of the relative density is ±0.5%.

grains confirmed their composition to be Y_2O_3. The elongated Y_2O_3 grains were randomly distributed within the matrix, with no relation to the loading direction. Higher magnification of the nanocrystalline grains revealed the presence of closed nanometric pores at many grain corners (arrowed in Fig. 6c).

After SPS at 1000 °C, a rather non-homogeneous microstructure was observed (Fig. 7), containing regions with micrometer size (~10 μm) and submicrometer size (500 nm) grains as well as pores. A lens-shaped LiF-rich second phase was observed at several grain boundaries (gb) of the larger grains (Fig. 7b), indicating a low solubility of LiF in Y_2O_3. The observed morphology of this second phase and the grain boundaries which were associated with it, resemble grain growth affected by Zener precipitate/pore drag.[31] The non-homogeneous microstructure observed after sintering of the LiF-added specimens, both at 700 °C and 1000 °C, may result from a very low volume fraction (2 vol%) of the LiF precursor crystals in nc-Y_2O_3, as well as from insufficient ball milling and the large particle size difference.
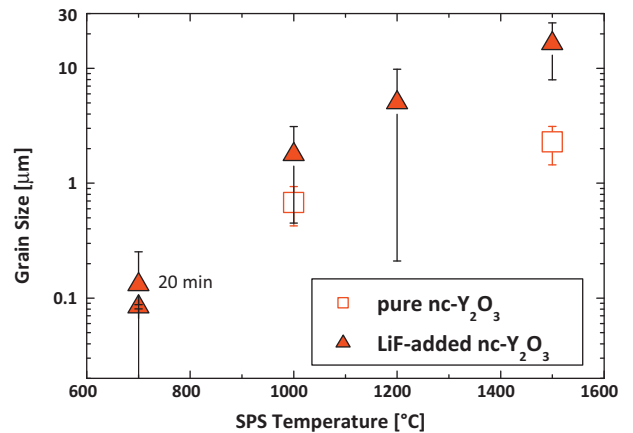

Fig. 5. Grain size after 5 min at the SPS temperature, plotted on a semilogarithmic scale, revealing the significant grain growth in the LiF-added nc-Y_2O_3 with the temperature increase. The average grain size increased from 84 ± 30 nm at 700 °C to 17 ± 10 μm at 1500 °C.
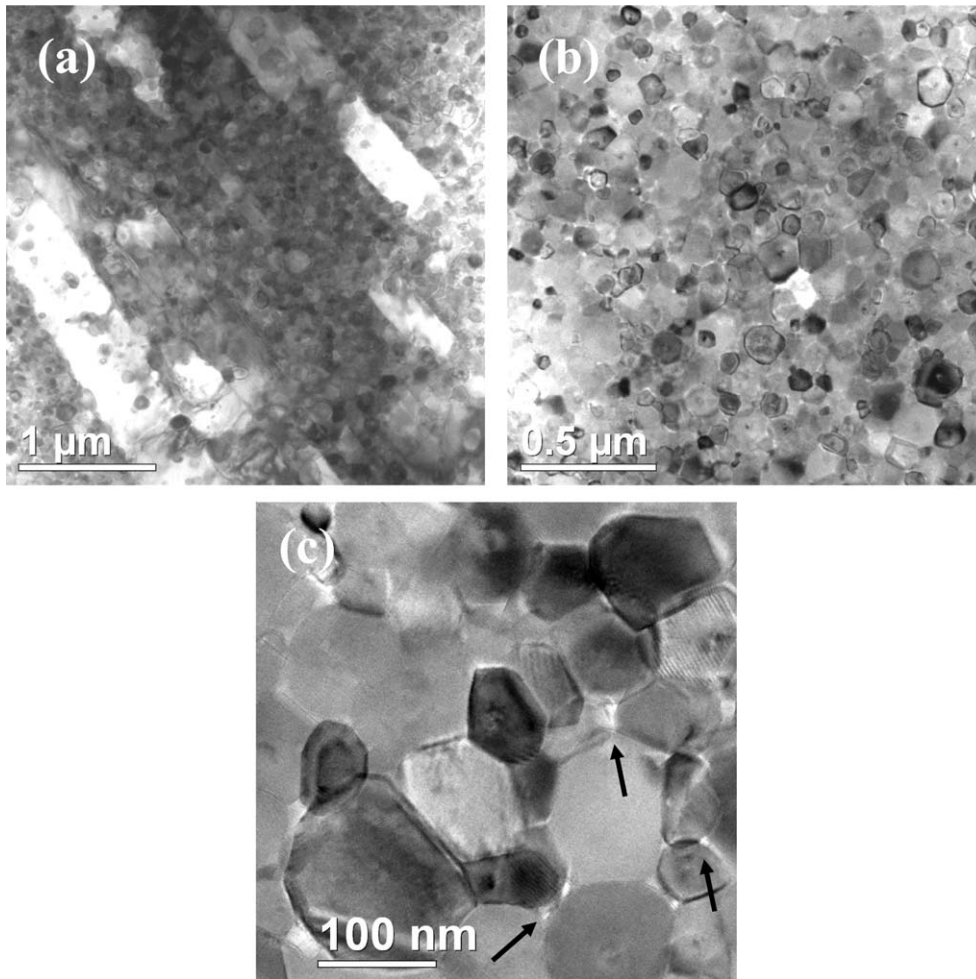
Fig. 6. TEM images from the 1 wt%LiF-added nc-Y$_2$O$_3$ after SPS at 700 °C for 5 min revealing (a) some micrometer size elongated grains in (b) the otherwise relatively homogeneous nanostructure matrix with equiaxed grains, smaller than 200 nm in diameter. (c) Closed nano-pores are visible at the nanometer-size grain corners (arrowed).

TEM images of specimens sintered at 1500 °C showed a more homogeneous microstructure with large micrometer-size grains (Fig. 8). Most of the grain boundaries in the LiF-added specimen were free of LiF-rich second-phase particles, which were occasionally observed as spherical globules occluded within the larger grains or at the gb quadruple nodes (Fig. 8a). The globular phase also appeared as pores inside the grains, apparently due to their preferred ion milling during the TEM specimen prepa-
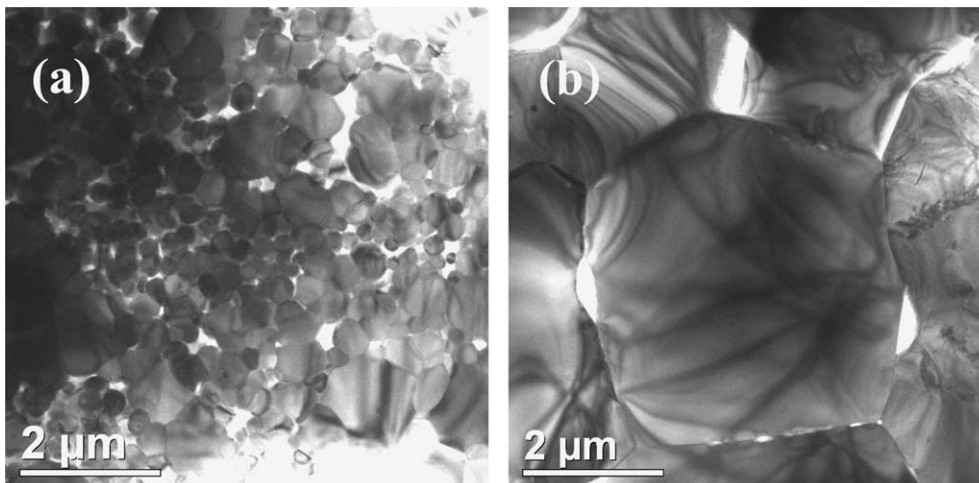

Fig. 7. TEM images showing the inhomogeneous grain and pore microstructure in the LiF-added nc-Y$_2$O$_3$ specimen after SPS at 1000 °C. (a) Matrix comprises of a mixture of nanometer and micrometer size grains. (b) LiF-rich lens-shaped second phase particles along the grain boundaries.
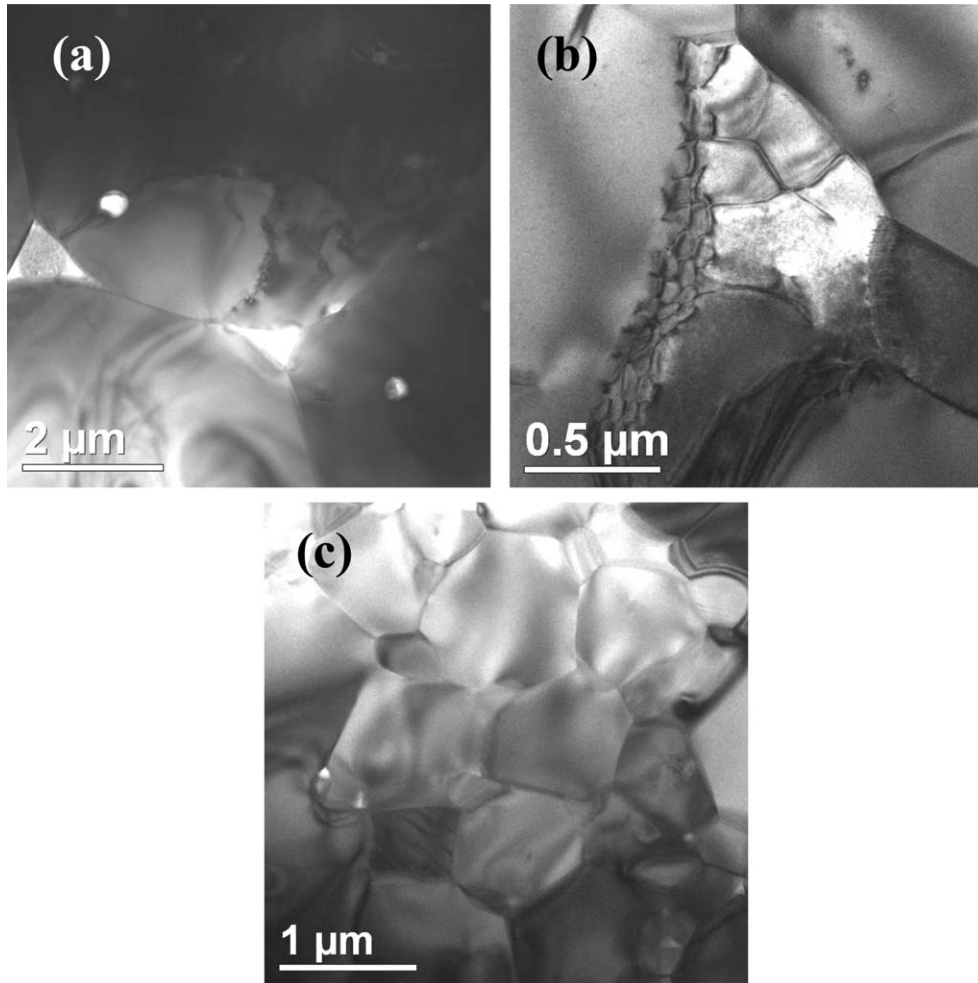
Fig. 8. TEM images showing the main microstructure features of the specimens sintered at 1500 °C by SPS. (a) LiF-rich globular occluded particles and amorphous gb phase at the corners of the larger dislocated grains in LiF-added nc-Y_2O_3. (b) Dislocation networks within the larger grains of pure Y_2O_3 versus (c) dislocation-free equiaxed submicrometer size grains.

ration. The second phase at the gb corners was featureless and exhibited an amorphous appearance; nevertheless, it was crystallized during the TEM observation (heated by the electron beam irradiation, i.e., the spherical particle at the triple junction at the left side of Fig. 8a), confirming the amorphous and metastable nature of the gb phase. The pores were distinguished from the second-phase particles and amorphous pockets by tilting experiments using TEM. Further microchemical composition analysis by EDS of the globular particles revealed the presence of a fluoride compound; lithium was not detected because of the detection limit of the EDS detector. Therefore, the globular as well as the gb phase at the grain corners were believed to be residue of a LiF-rich phase, which segregated to the grain boundaries during sintering, in agreement with previous findings.[22,23] The other important microstructure feature was the presence of dislocation networks resembling low angle grain boundaries (LAGBs) inside several large grains in LiF-added (Fig. 8a) and in pure Y_2O_3 (Fig. 8b) specimens. For comparison, TEM images of the pure nc-Y_2O_3 specimen sintered at 1500 °C showed dislocation-free regions with submicrometer size grains (Fig. 8c). These observed dislocation networks are the remnant

of the high temperature strain releasing mechanisms associated with particle sliding and rotation through which larger grains evolve.

The differential scanning calorimetric curves of the pure nc-Y_2O_3 and its LiF-added counterpart are shown in Fig. 9. The pure nc-Y_2O_3 exhibited a slight heat absorption with the temperature increase, which may be associated with partial sintering. However, very large endothermic peak spanning from ~400 °C to 1400 °C with a maximum around 1180 °C was observed in the LiF-added powder. This endothermic peak may be associated with reaction between the highly active surfaces of the nc-Y_2O_3 and viscous LiF or its constituents vapor, as LiF experiences drastic softening at 400 °C.[24] Finally, a small endothermic peak (hatched area in Fig. 9) overrides the larger peak, starting from the LiF melting temperature (~846 °C) and ending at ~985 °C, and resembles the LiF melting.

4. Discussion

All the SPS experiments confirmed that densification starts immediately as pressure is applied to the cold powder, pre-
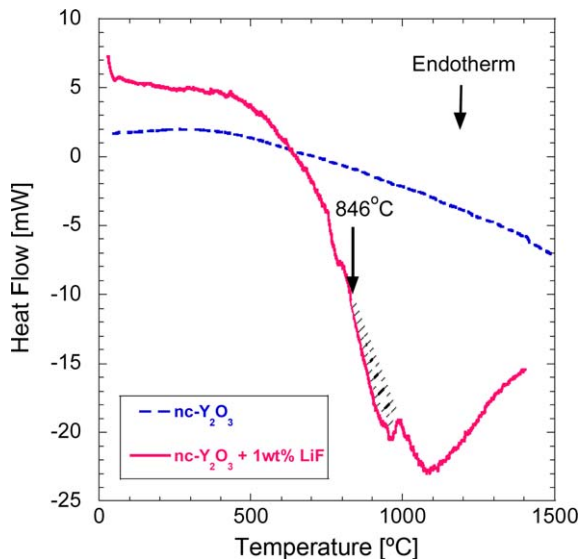
Fig. 9. Differential scanning calorimeter curves showing the endothermic reaction in 1 wt% LiF added nc-Y$_2$O$_3$ powder extending from 400 °C to 1400 °C, together with the endothermic melting peak of LiF (hatched peak). The LiF melting point (846 °C) is shown by the arrow.

sumably by particle rearrangement and sliding. A further rapid increase in the density occurs with the temperature increase, as was observed for the specimens sintered at 700 °C and 1000 °C. This further increase occurs by the aid of diffusional processes. Yet, this increase takes place to a larger extent and at a lower temperature for the LiF-added specimen than for pure nc-Y$_2$O$_3$ compact. As was mentioned above, LiF has been used as an effective sintering aid for densification of yttrium oxide to optical transparency.[22] However, densification of 1 μm size Y$_2$O$_3$ particles with LiF additive necessitated application of vacuum hot-pressing at high temperatures, i.e., 1300 °C. Full densification of 1–6 μm size particles also with LiF at lower temperatures, i.e., 950 °C and 70 MPa, was possible only after very long durations, up to 48 h.[23] In all reported experiments, a pressure of several tens of MPa was applied at the hot-pressing temperature. Therefore, the effect of LiF on enhanced densification in the present nanocrystalline powders should be carefully examined.

On one hand, LiF single crystals undergo an easy slip already at room temperature under a relatively low applied pressure of 3.4 MPa.[24] A deformation mechanism map for coarse grained LiF clearly indicates massive plastic deformation above 100 °C.[32] Our preliminary SPS experiments (not shown here), using the pure green compact of the present LiF microcrystals, showed significant plastic flow under 100 MPa already at room temperature, leading to almost full densification at 500 °C. LiF single crystals easily deform under compression of 1.4 MPa at 500 °C and 0.7 MPa at 700 °C.[24] This is expected to enhance the densification of the nc-Y$_2$O$_3$ powder compact in the vicinity of the LiF particles, subjected to a low (6 MPa) holding pressure at 600 °C. The large elongated Y$_2$O$_3$ grains observed at 700 °C can be a manifestation of this process. Nevertheless, the Y$_2$O$_3$ nanoparticles were evenly compacted at 700 °C into a dense structure throughout the specimens. Since the amount of 1 wt% (2 vol%) of LiF

microcrystals is not sufficient to be homogeneously distributed along all nc-Y$_2$O$_3$ grain boundaries, plastic deformation of LiF microcrystals alone cannot explain the enhanced densification at 700 °C.

On the other hand, similar enhanced and homogeneous densification was reported during low temperature (i.e., 575 °C) hot pressing of 100 nm MgO powder with 2 wt% LiF additive.[33] Their differential thermal analyses (DTA) showed no liquid formation at temperatures below the LiF melting point (846 °C). The authors deduced that if eutectic liquid forms, its composition and melting temperature should be very close to those of LiF. Consequently, the even distribution of LiF, below its melting point, throughout the powder compact was related to mass transfer by the vapor phase to facilitate particle rearrangement; the relatively high vapor pressure of 3×10^{-3} Pa was estimated at the hot-pressing temperature.[33] Similar evaporation of LiF and condensation on the Y$_2$O$_3$ nanoparticle surfaces may take place in the present system (see large endothermic peak in Fig. 9), albeit with much faster kinetics due to the higher heating rates and the applied electric field. In this respect, chemical reaction between LiF and the carbonic species such as sputtered carbon at the particle surfaces and CO gas present within the die atmosphere, may be responsible for the formation of gaseous graphite fluoride, (CF)$_n$, and Li ions, as suggested by Reimanis and Kleebe,[18] Meir et al.[19] and Nakajima.[34] The solubility of Li$^+$ ions in oxides such as spinel,[21,35] MgO,[14,36] and BaTiO$_3$[37] was reported. Adsorption of the very active Li$^+$ ions in the Y$_2$O$_3$ nanoparticle surfaces may enhance their surface activity, improve the surface diffusivity, and the wetting ability by forming point defects.[16,17] Surface modification may enable rapid shrinkage as it diminishes friction between particles, so that further compaction can take place. This is most important especially in nc-Y$_2$O$_3$, as was shown to experience a jamming effect in its pure composition. Therefore, enhanced densification aided by viscous flow and vapor condensation along the nanoparticle surfaces is in agreement with the very high shrinkage rates observed in the presence of LiF (i.e., 2.6×10^{-2} s^{-1}).

Furthermore, at temperatures above ~846 °C, LiF exists as a melt along the grain boundaries. At this stage, the available nc-Y$_2$O$_3$ particle surfaces may be modified by absorption of viscous LiF or its dissociated ions, and as a result of the small length-scale, high capillary force gradients may be present. Aside from this chemical driving force, additional electric field effects which enhance the diffusivity at the interfaces may also be present.[38,39] These effects apparently lead to accelerated diffusion, hence to much higher densification rates in the LiF-added specimens. The viscous LiF under the relatively high applied pressure (100 MPa) is thus distributed more evenly in the Y$_2$O$_3$ compact. According to hot-pressing experiments, the liquid LiF flows along surfaces and grain boundaries, into unfilled pores and finally towards the compact surfaces[33,40]; and is finally diminished by evaporation. Similar behavior was observed in the LiF-added yttria produced by hot forging where no LiF was detected using the flame photometry analysis.[23] However, the addition of LiF in the present study practically influences the SPS process of nc-Y$_2$O$_3$ at the lower temperature (700 °C) only, as it enables reaching the

final sintering stage (characterized by isolated pores and density >92%) within 5 min. This effect is highlighted by the much lower final density of 65% measured for the additive-free nc-Y_2O_3.

Once the melting temperature of LiF (846 °C) is reached, LiF can flow throughout the specimen, and enhance densification by modification of the particle surface and the grain boundary compositions. However, the specimens reach the dwell SPS temperatures when already at final stage sintering; further densification is prone to significant grain growth. Therefore, both the enhanced grain growth to the micrometer size grains, and the apparent low solubility of LiF, lead to LiF segregation as the second phase precipitates in the grain boundaries. This was the main reason for the degraded optical properties reported for increased hot-pressing temperatures in Y_2O_3; uneven distribution of LiF caused to abnormal grain growth and reduced optical transmittance.[22]

Finally, the non-homogeneous microstructure observed in the LiF-added specimens at low temperatures is due to the very low volume fraction of the LiF microcrystals dispersed within the Y_2O_3 nanoparticle matrix. In the regions adjacent to the LiF crystals, Y_2O_3 grain growth may be enhanced by immediate reaction with the viscous sintering additive. The LiF-rich regions at 1000 °C led to large micrometer-size grains, while neighboring LiF-lean regions remained in the submicrometer range. Higher SPS temperatures are also associated with faster chemical reaction of LiF with the carbonic gaseous atmosphere and decomposition of LiF as reported for spinel.[19,41] However, not all the LiF was able to leave the specimen. The occluded LiF-rich globules inside the grains, observed by TEM images, confirmed this. During the very rapid sintering process and due to the low solubility of LiF in Y_2O_3, excess LiF segregates to the grain boundaries and may be entrapped due to the higher mobility of the grain boundaries at high temperatures.

5. Conclusions

Nanocrystalline cubic yttria (nc-Y_2O_3) powder, with and without 1 wt% LiF as a sintering additive, were densified by spark plasma sintering at 100 MPa pressure, between 700 °C and 1500 °C. Sintering at 700 °C for 5 and 20 min durations in the presence of LiF resulted in 95% and 99.7% dense specimens; the corresponding grain sizes were 84 and 130 nm, respectively. The presence of LiF at low sintering temperatures assisted rapid densification by particle sliding and decreasing the jamming tendency. Higher sintering temperatures resulted in LiF segregation to the grain boundaries and its entrapment as a globular phase within the fast growing grains. The sintering enhancement advantage of LiF was lost at high temperatures, where enhanced grain growth took place.

Acknowledgments

References

1. Tokita M. Mechanism of spark plasma sintering and its application to ceramics. *Nyu Seramikkusu* 1997;**10**:43–53 [in Japanese].
2. Munir Z, Anselmi-Tamburini U, Ohyanagi M. The effect of electric field on the synthesis and consolidation of materials: a review of spark plasma sintering method. *J Mater Sci* 2006;**41**:763–77.
3. Nygren M, Shen Z. Spark plasma sintering: possibilities and limitations. *Key Eng Mater* 2004;**264–268**:719–24.
4. Chaim R. Densification mechanisms in spark plasma sintering of nanocrystalline ceramics. *Mater Sci Eng A* 2007;**443**:25–32.
5. Chesnaud A, Bogicevic C, Karolak F, Estournes C, Dezanneau G. Preparation of transparent oxyapatite ceramics by combined use of freeze-drying and spark plasma sintering. *Chem Commun* 2007:1550–2.
6. Li W, Gao L. Rapid sintering of nanocrystalline ZrO_2 (3Y) by spark plasma sintering. *J Eur Ceram Soc* 2000;**20**:2441–5.
7. Chaim R, Shen Z, Nygren M. Transparent nanocrystalline MgO by low temperature spark plasma sintering. In: *Ceramic nanomaterials and nanotechnology*. In: Song Wei Lu, Michael Z, HuYuri Gogotsi, editors. *Ceramic Transactions*, vol. 159. Westerville, Ohio: The ACerS Inc.; 2004. p. 21–30.
8. Chaim R, Marder-Jaeckel R, Shen JZ. Transparent YAG ceramics by surface softening of nanoparticles in spark plasma sintering. *Mater Sci Eng A* 2006;**429**:74–8.
9. Kim BN, Hiraga K, Morita K, Yoshida H. Spark plasma sintering of transparent alumina. *Scripta Mater* 2007;**57**:607–10.
10. Anselmi-Tamburini U, Woolman JN, Munir ZA. Transparent nanometric cubic and transparent zirconia obtained by high-pressure pulsed electric current sintering. *Adv Func Mater* 2007;**17**:3267–73.
11. Alaniz JE, Perez-Gutierrez FG, Aguilar G, Garay JE. Optical properties of transparent nanocrystalline yttria stabilized zirconia. *Opt Mater* 2009;**32**:62–8.
12. Yoon KJ, Kang SJL. Densification of ceramics containing entrapped gases during pressure sintering. *J Eur Ceram Soc* 1990;**6**:201–2.
13. Bernard-Granger G, Benameur N, Guizard C, Nygren M. Influence of graphite contamination on the optical properties of transparent spinel obtained by spark plasma sintering. *Scripta Mater* 2009;**60**:164–7.
14. Rhodes WH, Sellers DJ. Mechanism of pressure sintering MgO with LiF additions. *Am Ceram Soc Bull* 1967;**46**:469.
15. Rozenburg K, Reimanis IE, Kleebe HJ, Cook RL. Sintering kinetics of a $MgAl_2O_4$ spinel doped with LiF. *J Am Ceram Soc* 2008;**91**:444–50.
16. Wang MC, Wu NC, Yang S, Wen SB. Effect of LiF addition on the sintering of beta-spodumene precursor powders. *J Ceram Soc Jpn* 2002;**110**:149–54.
17. Fang Y, Agrawal D, Skandan D, Jain M. Fabrication of transparent MgO ceramics using nanopowders. *Mater Lett* 2004;**58**:551–4.
18. Reimanis IE, Kleebe HJ. A review on the sintering and microstructure development of transparent spinel ($MgAl_2O_4$). *J Am Ceram Soc* 2009;**92**:1472–80.
19. Meir S, Kalabukhov S, Froumin N, Dariel MP, Frage N. Synthesis and densification of transparent magnesium aluminate spinel by SPS processing. *J Am Ceram Soc* 2009;**92**:358–64.
20. Frage N, Kalabukhov S, Sverdlov N, Ezersky V, Dariel MP. Densification of transparent yttrium aluminum garnet (YAG) by SPS processing. *J Eur Ceram Soc* 2010;**30**:3331–7.
21. Villalobos GR, Sanghera JS, Aggrawal ID. Degradation of magnesium aluminum spinel by lithium fluoride sintering aid. *J Am Ceram Soc* 2005;**88**:1321–2.
22. Majima K, Niimi N, Watanabe M, Katsuyama S, Nagai H. Effect of LiF addition on the preparation of transparent Y_2O_3 by the vacuum hot pressing method. *J Alloys Compd* 1993;**193**:280–2.
23. Lefever RA, Matsko J. Transparent yttrium oxide ceramics. *Mater Res Bull* 1967;**2**:865–9.
24. Budworth DW, Pask JA. Flow stress on the {1 0 0} and {1 1 0} planes in LiF, and the plasticity of polycrystals. *J Am Ceram Soc* 1963;**46**:560–1.
25. Chaim R, Shlayer A, Estournes C. Densification of nanocrystalline Y_2O_3 ceramic powder by spark plasma sintering. *J Eur Ceram Soc* 2009;**29**:91–8.

26. Marder R, Chaim R, Estournes C. Grain growth stagnation in fully dense nanocrystalline Y_2O_3 by spark plasma sintering. *Mater Sci Eng A* 2010;**527**:1577–85.

27. Yoshida H, Morita K, Kim BN, Hiraga K, Kodo M, Soga K, Yamamoto T. Densification of nanocrystalline yttria by low temperature spark plasma sintering. *J Am Ceram Soc* 2008;**91**:1707–10.

28. He MS, Li JB, Lin H, Guo GR, Liang L. Fabrication of transparent polycrystalline yttria ceramics by combination of SPS and HIP. *J Rare Earth* 2006;**24**:222–4.

29. Cates ME, Wittmer JP, Bouchaud JP, Claudin P. Jamming, force chains, and fragile matter. *Phys Rev Lett* 1998;**81**:1841–4.

30. Valverde JM, Quintanilla MAS, Castellanos A. Jamming threshold for dry fine powders. *Phys Rev Lett* 2004;**92**:258303.

31. Sakarcan M, Hsueh CH, Evans AG. Experimental assessment of pore breakaway during sintering. *J Am Ceram Soc* 1983;**66**:456–61.

32. Verrall RA, Fields RJ, Ashby MF. Deformation-mechanism maps for LiF and NaCl. *J Am Ceram Soc* 1977;**60**:211–6.

33. Benecke MW, Olson NE, Pask JA. Effect of LiF on hot-pressing of MgO. *J Am Ceram Soc* 1967;**50**:365–8.

34. Nakajima T. Carbon–fluorine compounds as battery materials. *J Fluorine Chem* 1999;**100**:57–61.

35. Rozenburg K, Reimanis IE, Kleebe HJ, Cook RL. Chemical interaction between LiF and $MgAl_2O_4$ spinel during sintering. *J Am Ceram Soc* 2007;**90**:2038–42.

36. Wermuth FR, Knapp WJ. Initial sintering of MgO and LiF-doped MgO. *J Am Ceram Soc* 1973;**56**:401.

37. Wang SF, Yang TCK, Huebner W, Chu JP. Liquid-phase sintering and chemical inhomogeneity in the $BaTiO_3$–$BaCO_3$–LiF system. *J Mater Res* 2000;**15**:407–16.

38. Conrad H. Influence of an electric or magnetic field on the liquid–solid transformation in materials and on the microstructure of the solid. *Mater Sci Eng A* 2000;**287**:205–12.

39. Garay JE, Glade SC, Anselmi-Tamburini U, Asoka-Kumar P, Munir ZA. Electric current enhanced defect mobility in Ni_3Ti intermetallics. *Appl Phys Lett* 2004;**85**:573–5.

40. Hart PE, Atkin RB, Pask JA. Densification mechanisms in hot-pressing of magnesia with fugitive liquid. *J Am Ceram Soc* 1970;**53**:83–6.

41. Huang JL, Sun SY, Chen CY. Investigation of high alumina spinel: effects of LiF and $CaCO_3$ addition (part2). *Mater Sci Eng A* 1999;**259**:1–7.